Materials Research Letters

ISSN: (Print) (Online) Journal homepage: www.tandfonline.com/journals/tmrl20

Rapid precipitation of $L1_2$ phase in $Al_{0.5}CoCrFeNi$ high-entropy alloy under electropulsing

Zhicheng Wu, Xiaofeng Xu, Lai Wei, Yongqiang Yu, Xingguo Fu, Ganghu Cheng, Hailong Jia & Yue Jiang

To cite this article: Zhicheng Wu, Xiaofeng Xu, Lai Wei, Yongqiang Yu, Xingguo Fu, Ganghu Cheng, Hailong Jia & Yue Jiang (28 Feb 2025): Rapid precipitation of $L1_2$ phase in $Al_{0.5}CoCrFeNi$ high-entropy alloy under electropulsing, Materials Research Letters, DOI: 10.1080/21663831.2025.2471963

To link to this article: https://doi.org/10.1080/21663831.2025.2471963

MATER. RES. LETT.
https://doi.org/10.1080/21663831.2025.2471963

MATERIALS RESEARCH LETTERS
Taylor & Francis
Taylor & Francis Group

REPORT

Rapid precipitation of $L1_2$ phase in $Al_{0.5}CoCrFeNi$ high-entropy alloy under electropulsing

Zhicheng Wu[a], Xiaofeng Xu[a,b], Lai Wei[a], Yongqiang Yu[a], Xingguo Fu[a], Ganghu Cheng[a], Hailong Jia[a] and Yue Jiang[b,c]

[a]Key Laboratory of Automobile Materials, Ministry of Education, and Department of Materials Science and Engineering, Jilin University, Changchun, People's Republic of China; [b]National Key Laboratory of Automotive Chassis Integration and Bionic, Jilin University, Changchun, People's Republic of China; [c]Key Laboratory of Bionic Engineering of Ministry of Education, College of Biological and Agricultural Engineering, Jilin University, Changchun, People's Republic of China

ABSTRACT

A new strategy for the rapid precipitation (1.8 s) of $L1_2$ nanoprecipitates in $Al_{0.5}CoCrFeNi$ high-entropy alloys by electropulsing treatment (EPT) has recently been discovered. The coherent $L1_2$ phase was introduced under high temperatures by EPT, and this result broke the previous understanding that it needs to be aged for a long time at low temperatures. The formation of the $L1_2$ precipitates was mainly attributed to the combination of thermal and athermal effects during EPT. This work provides insights into the rapid regulation of multiphase (FCC + B2 + $L1_2$) and dislocation combinations in high-entropy alloys to optimize strength and ductility.

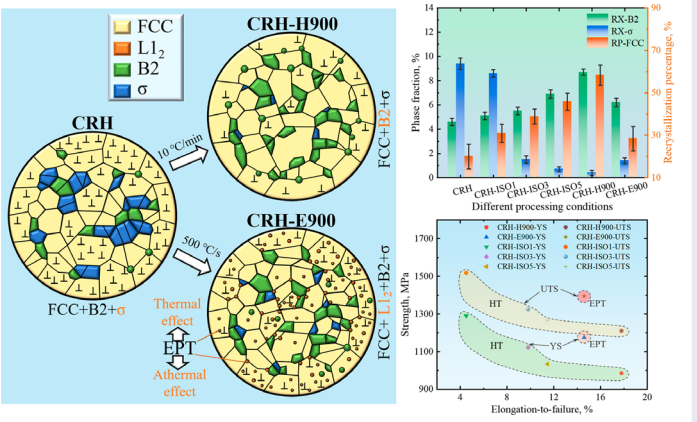

ARTICLE HISTORY
Received 13 November 2024

KEYWORDS
High-entropy alloy; electropulsing; $L1_2$ nanoprecipitate; dislocation

IMPACT STATEMENT

During electropulsing treatment, the coherent $L1_2$ phase was introduced quickly in $Al_{0.5}CoCrFeNi$ high-entropy alloys, achieving a better combination of strength and ductility beyond the region of HT.

1. Introduction

Recently, high-entropy alloys (HEAs) have received widespread attention from researchers due to outstanding fracture toughness and exceptional ductility [1,2]. Compared to single-phase HEA with low yield strength, $Al_xCoCrFeNi$ HEAs with FCC + BCC ($0.4 < x < 0.9$) exhibit high strength, which can be potential structural materials in extreme environments [3–7]. Thereinto, $Al_{0.5}CoCrFeNi$ is an FCC + BCC HEA with both high strength and excellent strain-hardening ability [8]. During conventional heat treatment (HT), different phases prefer precipitating at various temperatures. The phase compositions of the $Al_{0.5}CoCrFeNi$ alloy are $L1_2$ + BCC+σ (< 600 °C), FCC + B2+σ (600-800 °C)

CONTACT Xiaofeng Xu xuxiaofeng@jlu.edu.cn Key Laboratory of Automobile Materials, Ministry of Education, and Department of Materials Science and Engineering, Jilin University, 130025, Changchun, People's Republic of China; National Key Laboratory of Automotive Chassis Integration and Bionic, Jilin University, 130025, Changchun, People's Republic of China

Supplemental data for this article can be accessed online at https://doi.org/10.1080/21663831.2025.2471963

and FCC + B2 (800-1300 °C) [6,8]. Generally, in addition to dislocation strengthening, the strengthening effect is mainly rooted in the contribution of the B2 phase and $L1_2$ nanoprecipitate in multiphase HEAs [9–11].

The $L1_2$ nanoprecipitate can better balance strength and ductility in contrast with the B2 phase [6–8,12]. Al_xCoCrFeNi HEA tends to form Al-Ni-rich precipitates to maintain a more stable state during heat treatment [8,13]. Due to differences in precipitation sequences and atomic diffusion rate, the B2 phase can be formed within 1 h during annealing (> 800 °C) [3,9], and the $L1_2$ phase can only be obtained during 4–200 h ageing (< 800 °C) in the fully recrystallized Al-Co-Cr-Fe-Ni-Ti alloys [6–8,12]. The formation of the $L1_2$ phase is influenced by element content (e.g. Al, Ti) [11,14], temperature and thermomechanical processing route [8,9]. The early precipitation stage of the $L1_2$ phase mainly involves the classical nucleation mechanism [9,15–17] and spinodal decomposition of supersaturated solid solution [10,18]. It has been reported that $L1_2$ precipitates cannot be formed after cold rolling and low temperature annealing, and conventional solution treatment (∼ 1200 °C) is required before annealing to subsequently generate $L1_2$ precipitates, slowing down the precipitation kinetics [8,9]. Simultaneously, severe lattice distortion and sluggish diffusion effects in the HEA matrix retard the precipitation kinetics of the $L1_2$ phase [6–12,19,20]. Accordingly, the $L1_2$ phase cannot be formed quickly due to the low atomic diffusion rate under the low-temperature by one-step HT. Generally, the phase transformation temperature increases with increasing heating rate [21–23], and the higher temperature and faster element diffusion rate during heating may accelerate the formation of the $L1_2$ phase. Obviously, the combination of high temperature (> 800 °C) and rapid heating rate cannot be obtained under HT. In addition, there are almost no reports on the microstructure evolution of the $L1_2$ phase under high heating rates [6–12]. Therefore, it is necessary to find a new strategy for the rapid formation of $L1_2$ nanoprecipitates.

Electropulsing treatment (EPT) with a speedy heating rate can effectively improve the microstructure and mechanical properties of alloys by means of accelerated recrystallization [24], rapid phase transformation [25], electroplasticity [26], and accelerated precipitation [27,28]. Moreover, EPT has been reported to significantly improve vacancy and atomic motion rates, reducing the nucleation energy barrier of precipitates [29,30]. Therefore, EPT may be a feasible strategy to accelerate the formation of the $L1_2$ phase, thereby manipulating the multiphase combination (FCC + B2 + $L1_2$) to optimize the strength-ductility of HEA quickly. Unfortunately, after a review of the relevant studies, there is little research on the evolution of the $L1_2$ phase in HEA via EPT.

In this work, we successfully used one-step EPT in $Al_{0.5}$CoCrFeNi HEA to make the $L1_2$ and B2 phases precipitate rapidly, avoiding the long-term low-temperature ageing of traditional heat treatment. The multiphase combination of low-temperature and high-temperature phases was quickly achieved in partially recrystallized HEA. This work also attempts to reveal the rapid formation mechanism of the $L1_2$ phase under EPT through microstructure analysis.

2. Experimental material and procedures

The as-cast $Al_{0.5}$CoCrFeNi HEA samples (at.%: 10.82Al, 22.05Co, 22.82Cr, 22.03Fe, 22.25Ni) were homogenized at 1200 °C for 6 h under protective gas before water-quenching, then cold-rolling (∼ 78% reduction) at room temperature. The cold-rolled (CR) plates were processed into samples of 45 × 10 × 1 mm. The experimental details are shown in Supplementary Figure S1. The cold-rolled samples at room temperature were directly heated to 800 °C using HT with 10 °C/min followed by water quenching, named the CRH sample (Supplementary Figure S1a). A computer-controlled self-made electropulsing device can produce 50 Hz alternating currents (Supplementary Figure S1b). The direction of the pulse current with a maximum current density of $\sim 2.9 \times 10^7$ A/m^2 was along the cold-rolled direction. The temperature change during EPT was observed using an infrared thermometer (ABSD-3014, response time 10 ms). The CRH samples at room temperature were heated to 900 °C with HT (∼ 10 °C/min for ∼ 87.5 min) and EPT (∼ 500 °C/s for ∼ 1.8 s) and then immediately water-cooled, named CRH-H900 and CRH-E900, respectively. Subsequently, the CRH-ISO process was adopted to further increase the heating rate and shorten the time, comprehensively exploring the differences in microstructure and mechanical properties caused by HT and EPT. The CRH samples at room temperature were directly isothermally treated at 900 °C using HT for 1.3, 3, and 5 min, and then immediately water-cooled, named CRH-ISO1, CRH-ISO3 and CRH-ISO5, respectively. In particular, the heating rate for CRH-ISO1 was ∼ 11 °C/s (1.3 min).

The microstructure of the samples was observed using scanning electron microscopy (SEM, TESCAN VEGA3), electron backscattered diffraction (EBSD, Oxford Symmetry detector) on the SEM (JSM-7900F). The chemical compositions (at.%) of the samples were determined by the energy dispersive spectrometer (EDS, Oxford X-Max). The transmission electron microscopy (TEM, JEM-2100F) was used to investigate the substructure at 200 kV. The MTS-810 testing machine equipped with

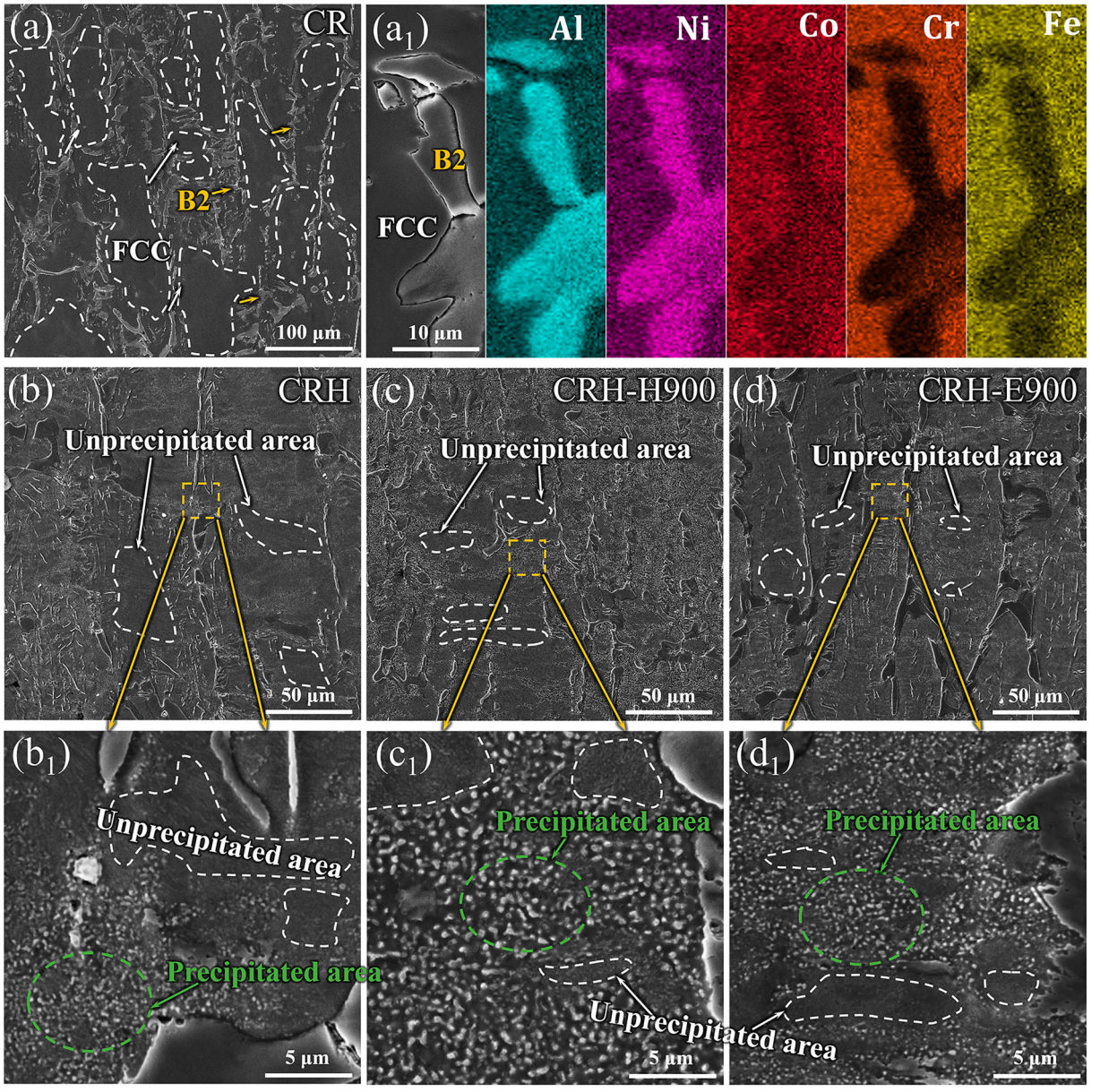

Figure 1. SEM and EDS images of (a, a_1) CR, (b, b_1) CRH, (c, c_1) CRH-H900 and (d, d_1) CRH-E900. (a_1-d_1) are high-magnification SEM images taken from (a-d).

a mechanical extensometer with a gauge dimension of 10 mm was used to conduct three tensile tests at a strain rate of 10^{-3} s^{-1} at room temperature on different samples. The width and thickness of the middle parallel end of the tensile specimen were 2 and 1 mm, respectively. The loading direction was along the cold-rolled direction.

3. Results and discussion

The metallographic topography is observed by SEM before and after EPT. Figure 1 (a, a_1) shows the FCC + B2 (Al and Ni-rich) dual-phase microstructure of the rolled sample, in which the B2 phase is coarse and no fine precipitates are found. After annealing, the unprecipitated and precipitated areas appear in the CRH sample and the fine precipitate phases can be observed in the precipitated area (Figure 1b, b_1). Both CRH-H900 and CRH-E900 samples show increased precipitation area (Figure 1 (c, c_1), (d, d_1)). It is noteworthy that the size of the precipitates in the CRH-E900 sample is significantly lower than that of CRH-H900 (Figure 1 c_1, d_1).

The evolution of the microstructure before and after EPT is carefully studied using EBSD analysis. Figure 2 (a, a_1)-(c, c_1) shows the microstructure of the different samples, which can be divided into the complete recrystallization region (RX) and unrecrystallization region (URX). The RX is composed of FCC + B2+σ phases in

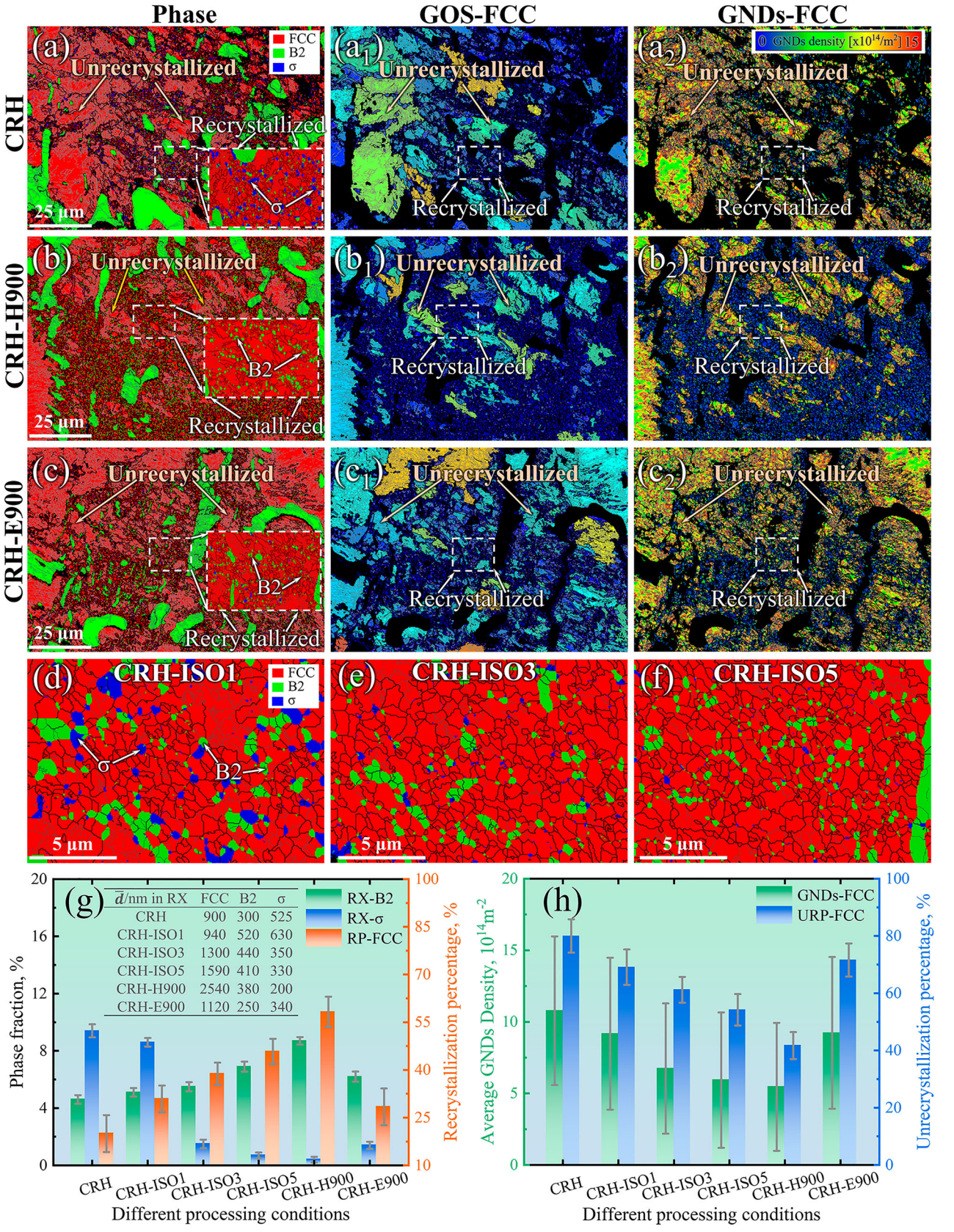

$\bar{d}$/nm in RX	FCC	B2	σ
CRH	900	300	525
CRH-ISO1	940	520	630
CRH-ISO3	1300	440	350
CRH-ISO5	1590	410	330
CRH-H900	2540	380	200
CRH-E900	1120	250	340

Figure 2. EBSD Phase, grain orientation spread (GOS) and GNDs maps of (a-a_2) CRH, (b-b_2) CRH-H900 and (c-c_2) CRH-E900. EBSD Phase maps (in the RX) of (d) CRH-ISO1, (e) CRH-ISO3 and (f) CRH-ISO5. (g) The average phase fraction (RX-B2, RX-σ) and size ($\bar{d}$) of B2 and σ phases in the recrystallization zone (excluding B2 precipitates with a diameter greater than 1 μm), (g, h) the recrystallization and unrecrystallization percentage (RP-FCC, URP-FCC) and GNDs density of the FCC phase.

the various samples (Figure 2a-f). For CRH-H900 and CRH-E900 samples, the recrystallization percentage of FCC phase (RP-FCC) increases compared to CRH, and the phase fraction of B2 (RX-B2) and σ (RX-σ) phases in the RX increases and decreases significantly, respectively (Figure 2g). CRH-H900 shows higher RP-FCC and RX-B2 while lower RX-σ than CRH-E900 due to the longer heating time (Figure 2g). Moreover, the average FCC and B2 phase sizes ($\bar{d}$) in RX of CRH-E900 are smaller while σ is coarser than those of CRH-H900 due to shorter heating time (Table in Figure 2g). For CRH-ISO1 $\sim$ 5, the RP-FCC and RX-B2 increase while RX-σ decreases with increasing isothermal treatment time, which is between CRH and CRH-H900 (Figure 2d-g). Whereas the average B2 and σ sizes in the RX of CRH-ISO1 are the coarsest compared to the other samples (Table in Figure 2g), implying the growth of the original precipitate dominates due to shorter time (1.3 min). The precipitation of the B2 phase and the dissolution of the σ phase occur simultaneously during rapid EPT of 1.8 s, so the average B2 and σ sizes of CRH-E900 in RX are smaller than those in CRH-ISO1 (Figure 2g). Besides, the URX contains high geometrically necessary dislocations (GNDs) (Figure 2a_2-c_2). After HT and EPT, the GNDs and URP-FCC decrease in contrast with CRH (Figure 2h).

The evolution of microstructure before and after EPT is ultimately determined by TEM analysis (Figure 3). The CRH sample is composed of RX and URX, the FCC+ B2+σ (Cr-rich) phases in RX can be determined by EDS and SAED, and the atomic ratio of Al and Ni in the B2 precipitates is 1:1 (Figure 3a, a_1-a_3). The $L1_2$ phase is not found. In contrast with CRH, the CRH-H900 sample consists of a higher proportion of RX (Figure 2a, b) with FCC + B2+σ phases (Figure 3b, b_1). For the CRH-E900 sample, the FCC+σ+B2 phases are also found in the RX (Figure 3c, c_1-c_3). However, it should be noted that no element enrichment is found in the URX of CRH and CRH-H900 (Figure 3 (a, a_1), (b_1, b_2)). Conversely, EDS analysis shows that a large amount of Al and Ni-rich nanoprecipitates are distributed in the URX of the CRH-E900 sample (Figure 3 (c, c_1), (d, d_3)). The atomic ratio of (Ni + Co):Al is close to 3:1 (Figure 3d_3, e), which indicates that the nanoprecipitates are $L1_2$ phase [10]. In addition, Figure 3 (d_1, d_2) shows the [111] and [112] FCC zone axis (ZA) with extra super-lattice reflections (yellow circle mark), indicating the presence of the $L1_2$ phase [9]. The HAADF-STEM image in Figure 3d_3 shows the uniform distribution of $L1_2$ precipitates in URX, and the $L1_2$ nanoprecipitates are also found at the grain boundaries and intragranular regions in RX (Figure 3e, e_1, e_2).

The precipitation of alloys is a diffusion-controlled process [31]. The Al atoms with a larger radius cause severe lattice distortion in the matrix of Al-Co-Cr-Fe-Ni HEA, resulting in a slow diffusion of the elements [6,19]. Generally, the grain boundaries can serve as fast diffusion paths for elements, accelerating precipitation kinetics [32]. Thus, the grain boundaries can act as the main heterogeneous nucleation sites for the precipitates. During HT (800-900 °C), due to the differences in phase formation temperature and time, the B2 phase mainly precipitates heterogeneously at grain boundaries and the σ phase gradually dissolves, while the $L1_2$ phase does not appear (Figure 4a). Thus, the microstructure of CRH consists of the B2 phase, σ phase and incomplete recrystallization FCC grains (Figures 2a and 3a). For CRH-ISO1, the microstructure mainly involves the growth of the original σ and B2 phases due to the short heating time (Figure 2a, d, g). For CRH-H900, the microstructure evolution includes an increased RP-FCC, the heterogeneous precipitation of B2 and the dissolution of σ phase in the RX compared to CRH (Figure 2b, g).

However, a large number of $L1_2$ precipitates are found in the URX after CRH-E900, which is dissimilar from previous studies that the $L1_2$ phase can only be obtained at $<$ 800 °C (4–200 h ageing) [6–8]. EPT has a significant effect on the phase change pathway and temperature. It is well known that the phase transformation temperatures increase with increasing heating rate [21–23], so the phase diagram of the $L1_2$ phase will shift to a higher temperature under EPT with a high heating rate. Meanwhile, EPT can reduce the phase formation temperature by reducing the precipitation nucleation barrier [27,28]. It should be pointed out that the increased $L1_2$ phase transformation temperature caused by the rapid heating of EPT is dominant in this work. Consequently, the elements exhibit higher diffusion rates at higher $L1_2$ phase formation temperatures during EPT, reducing precipitation time. Simultaneously, the electronic wind generated by the EPT contributes to opening the dislocation tangle and increasing the atomic diffusion rate [33,34]. In addition, each atom in a high-entropy alloy has the potential to hinder the movement of free electrons to a greater extent, electrons scattering at a higher frequency, causing more local hot spots and higher atomic diffusion rates during EPT due to localized Joule heating [35–38]. Thus, the CRH-E900 shows a higher RP-FCC and lower dislocation density in contrast with the CRH. Meanwhile, the Al and Ni atoms have the smallest mixing enthalpy in $Al_{0.5}$CoCrFeNi HEA, tending to form an Al-Ni-rich precipitate to maintain a more stable state during heat treatment [8,13]. Therefore, the combined effect of thermal and athermal under EPT increases the atomic diffusion rate and promotes the rapid heterogeneous precipitation of $L1_2$ and B2 phases. The detailed dislocation evolution and $L1_2$ precipitate formation mechanism under EPT are

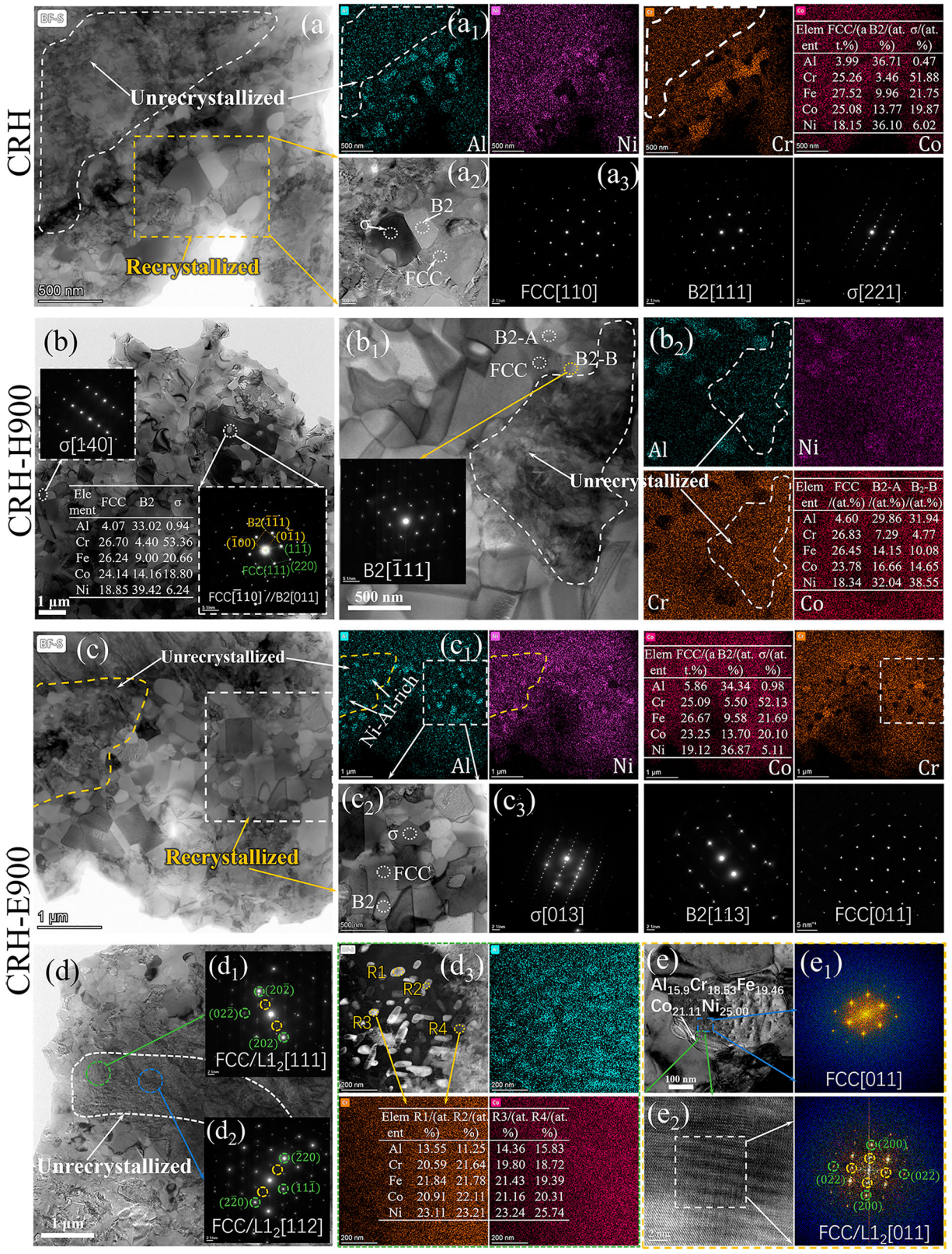

Figure 3. TEM bright field images (BF-S) and HAADF-STEM images (DF-S) with the corresponding SAED diagrams, EDS, and HRTEM patterns of (a-a_3) CRH, (b-b_2) CRH-H900 and (c-e) CRH-E900. (a_1), (b_2) and (c_1) correspond to (a), (b_1) and (c), respectively. (a_2) and (c_2) with the corresponding SAED diagrams (a_3) and (c_3) are taken from (a) and (c), respectively. (d_3) DF-S with the corresponding EDS is taken from the green wireframe of (d). (e_1) and (e_2) HRTEM (with the FFT patterns) are taken from (e).

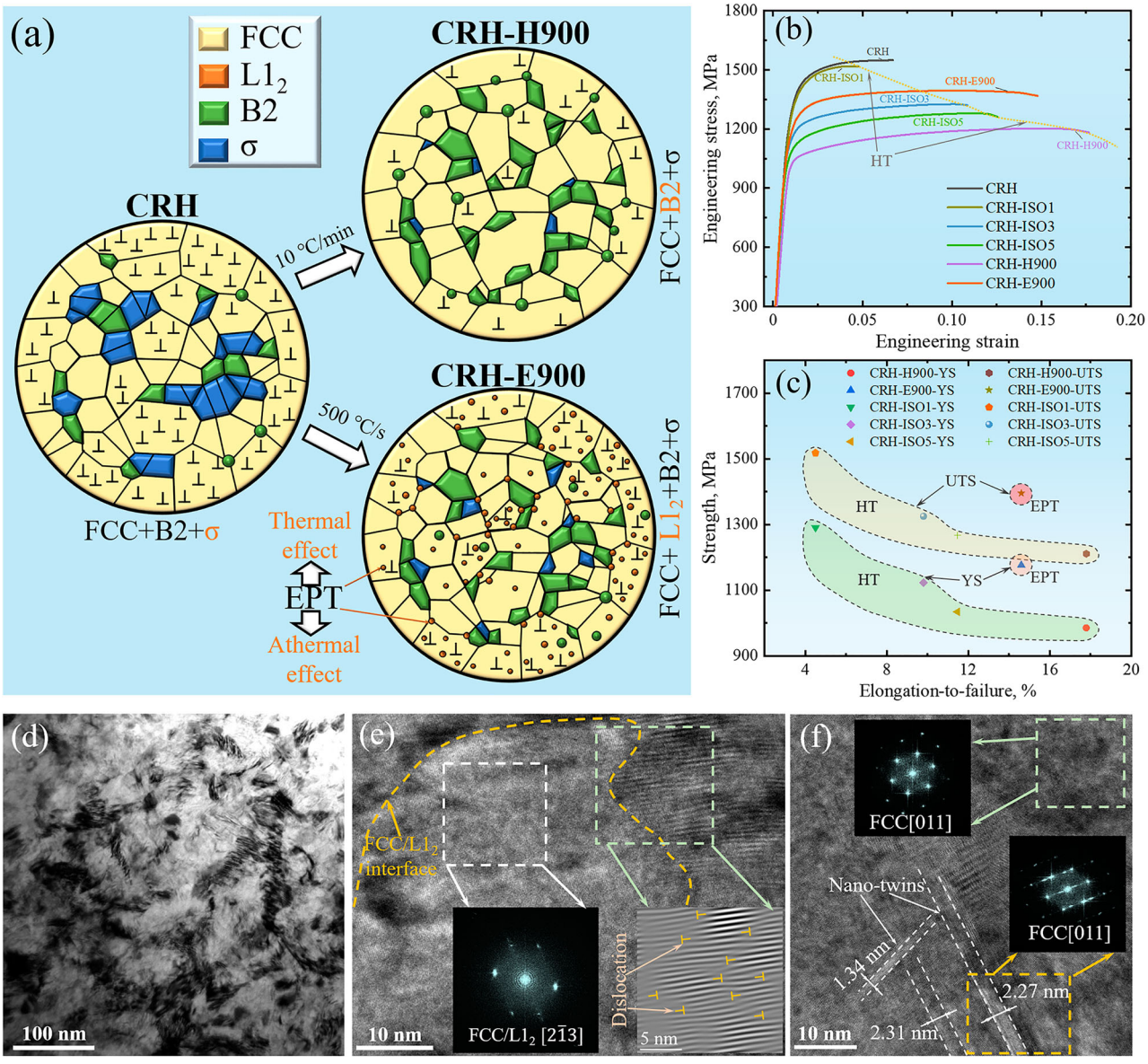

Figure 4. (a) Schematic diagram of precipitation evolution during EPT and HT. (b) Engineering stress-strain curves. (c) The strength and elongation-to-failure after various treatment conditions. (d) TEM BF, (e) and (f) HRTEM (with the corresponding FFT and inverse FFT images) patterns of the CRH-E900 sample after tensile testing.

shown in the Supplementary materials. In contrast, the σ precipitate is thermodynamically unstable under EPT, and tends to dissolve to maintain the thermodynamic stability of the system [39].

In addition, the normalized nucleation barrier of the $L1_2$ phase is lower, attributed to the low γ (FCC/$L1_2$) coherent interfacial energy of 8–24 mJ/m^2 [40,41], while the B2 (BCC) phase (180-450 mJ/m^2) and σ phase (500-800 mJ/m^2) have higher nucleation barrier [42,43]. Thus, the $L1_2$ phase with a lower nucleation barrier is easier to form in comparison to the competing B2 phase, and many $L1_2$ precipitates are found at the grain boundary of RX and the dislocation region of URX after EPT (Figure 3c-e). Besides, the higher element diffusion rate caused by EPT (rooting in the energy fluctuations and electron current) leads to the precipitation of the $L1_2$ phase at intragranular regions (with a higher nucleation energy barrier). Correspondingly, RX-B2 of CRH-E900 is slightly lower than CRH-H900, but significantly higher than that of CRH-ISO1, 3 (Figure 2g). Additionally, CRH-E900 with an extremely short time leads to a higher URP and GNDs, while the average sizes of B2 and FCC phases in RX are smaller compared with CRH-H900 (Figures 2g and 4a). Contrasted with the phase-equilibrium state of the phase diagram of HT, the $L1_2$ phase obtained during EPT is metastable precipitates with low Al atomic fraction (at.%: ~15) due to the very short duration. Overall, the phase evolution under CRH-E900 conditions

simultaneously involves the recrystallization of fine FCC grains, the precipitation of B2 and $L1_2$, and the dissolution of σ phases (Figure 4a). It is noteworthy that EPT breaks the original precipitation sequence and establishes a new precipitation competition relationship, so that the rapid formation of $L1_2$ nanoprecipitates under EPT breaks the previous understanding that long-term ageing at low temperatures is required.

Figure 4 (b, c) shows the tensile mechanical properties of the samples before and after EPT. The yield strength (YS) and ultimate tensile strength (UTS) are ~1.18 GPa and ~1.39 GPa for CRH-E900, ~985 MPa and ~1.21 GPa for CRH-H900, respectively. The elongation-to-failure (EL) of the CRH-E900 (~14.6%) sample is remarkably improved compared to the CRH sample (~7.0%). The differences in strength and ductility of different samples are attributed to the strengthening and strain contributions of FCC matrix, precipitates and dislocations. The strain contributions of HEAs are mainly attributable to the FCC matrix and coherent $L1_2$ phases, while the harder semi-coherent/incoherent B2 and σ phases show almost no contribution [6,8,20,44–46]. The YS of CRH-E900 increased by ~191 MPa compared to CRH-H900, attributed to higher dislocation and $L1_2$ strengthening, and the EL is slightly lower. For CRH and CRH-ISO1 samples, although high dislocation density and RX-σ can improve strength, dislocations, especially the coarse σ phase (Figure 2d), significantly reduce the ductility (~4.5%) of CRH-ISO1. Thereinto, the σ phase is a brittle precipitate and grain boundaries are its heterogeneous nucleation sites due to the high nucleation barrier [43]. However, coarse σ precipitates are considered the site of crack initiation and propagation, significantly reducing ductility [46]. Compared with CRH and CRH-ISO1 specimens, the YS of CRH-E900 only decreased by ~9.9% and ~8.8%, while the EL increased by ~109% and ~224%, respectively. Interestingly, the CRH-E900 specimen shows lower RP-FCC and higher dislocation density than those of CRH-ISO3 and CRH-ISO5 (Figure 2g, h), but the strength and ductility increase simultaneously (Figure 4c). It is well known that lower RP-FCC and higher dislocation density will lead to lower ductility [7,24], which contradicts the result of CRH-E900. For the above results, the $L1_2$ phase plays a crucial role. On the one hand, the formation of the $L1_2$ phase effectively alleviates the severe dislocation accumulation and strain localization in the URX, and effectively resists the dislocation motion during the subsequent deformation process [8,20]. On the other hand, the precipitation-free region (Ni-Al-poor) near the FCC/$L1_2$ and FCC/B2 phase interface can act as a storage site for dislocation and tend to form stacking faults and nano-twins during deformation, thereby improving the strain hardening capacity [47,48]. TEM BF and HRTEM of the CRH-E900 sample after the tensile test are shown in Figure 4d-f. A large number of dislocation entanglements and nano-twins appear in the precipitation-free region near the precipitates (Figure 4d). The high density of dislocations exists at the FCC/$L1_2$ interface through the inverse FFT image (Figure 4e), and the width of partial nano-twins near the precipitates is 1.34–2.31 nm (Figure 4f). It is worth noting that the coherent $L1_2$ nanoprecipitates can improve the strength and better coordinate the plastic deformation of the alloy [8–10], breaking the previous understanding of lower ductility at higher dislocation density. Accordingly, EPT is a feasible strategy to rapidly regulate the combination of multiphase (FCC + B2 + $L1_2$) and dislocations, achieving a better combination of strength and ductility beyond the strength-ductility region of HT (Figure 4b, c).

4. Conclusions

In summary, the rapid precipitation behavior of the $L1_2$ phase induced by EPT in $Al_{0.5}CoCrFeNi$ HEA has been studied in this work. Different from the dual-phase microstructure (FCC + B2) under HT, the multiphase structure (FCC + B2 + $L1_2$) can be quickly obtained by the thermal and athermal effects under EPT. The $L1_2$ nanoprecipitates are distributed in the RX and URX during EPT. The trade-off between the strength and ductility of HEAs can be quickly reconciled by the combined effect of multiphase (FCC + B2 + $L1_2$) and dislocations. Notably, EPT with electric-thermal field coupling brings more possibilities for microstructure regulation of HEAs systems, thereby tapping the potential of alloys to better meet industrial applications.

Disclosure statement

No potential conflict of interest was reported by the author(s).

Funding

Financial support from the National Natural Science Foundation of China (General Program: 52371030), Key Research and Development Program of Jilin (No. 20230201158GX), Provincial Natural Science Foundation of Shandong (No. ZR202102220408).

References

[1] Cantor B, Chang ITH, Knight P, et al. Microstructural development in equiatomic multicomponent alloys. Mater Sci Eng, A. 2004;375–377:213–218. doi:10.1016/j.msea.2003.10.257

[2] Li ZM, Pradeep KG, Deng Y, et al. Metastable high-entropy dual-phase alloys overcome the strength-ductility trade-off. Nature. 2016;534 (7606):227–230. doi:10.1038/nature17981

[3] Wu QF, Jia YH, Wang ZJ, et al. Rapid alloy design from superior eutectic high-entropy alloys. Scr Mater. 2022;219:114875. doi:10.1016/j.scriptamat.2022.114875

[4] Gao XZ, Lu YP, Zhang B, et al. Microstructural origins of high strength and high ductility in an $AlCoCrFeNi_{2.1}$ eutectic high-entropy alloy. Acta Mater. 2017;141:59–66. doi:10.1016/j.actamat.2017.07.041

[5] Bai X, Fang W, Chang RB, et al. Effects of Al and Ti additions on precipitation behavior and mechanical properties of $Co_{35}Cr_{25}Fe_{40-x}Ni_x$ TRIP high entropy alloys. Mater Sci Eng, A. 2019;767:138403. doi:10.1016/j.msea.2019.138403

[6] Rao JC, Diao HY, Ocelík V, et al. Secondary phases in Al CoCrFeNi high-entropy alloys: An in-situ TEM heating study and thermodynamic appraisal. Acta Mater. 2017;131:206–220. doi:10.1016/j.actamat.2017.03.066

[7] Kao YF, Chen TJ, Chen SK, et al. Microstructure and mechanical property of as-cast, -homogenized, and -deformed $Al_xCoCrFeNi$ ($0 \leq x \leq 2$) high-entropy alloys. J Alloys Compd. 2009;488 (1):57–64. doi:10.1016/j.jallcom.2009.08.090

[8] Yang HX, Li JS, Pan XY, et al. Nanophase precipitation and strengthening in a dual-phase $Al_{0.5}CoCrFeNi$ high-entropy alloy. J Met Sci Technol. 2021;72:1–7. doi:10.1016/j.jmst.2020.02.069

[9] Gwalani B, Gorsse S, Choudhuri D, et al. Modifying transformation pathways in high entropy alloys or complex concentrated alloys via thermo-mechanical processing. Acta Mater. 2018;153:169–185. doi:10.1016/j.actamat.2018.05.009

[10] Li W, Wang W, Niuc MC, et al. Unraveling the two-stage precipitation mechanism in a hierarchical-structured fcc/$L2_1$ high-entropy alloy: Experiments and analytical modeling. Acta Mater. 2024;262:119426. doi:10.1016/j.actamat.2023.119426

[11] Chen D, He F, Han B, et al. Synergistic effect of Ti and Al on $L1_2$-phase design in CoCrFeNi-based high entropy alloys. Intermetallics. 2019;110:106476. doi:10.1016/j.intermet.2019.106476

[12] Gwalani B, Gangireddy S, Zheng YF, et al. Influence of ordered $L1_2$ precipitation on strain-rate dependent mechanical behavior in a eutectic high entropy alloy. Sci Rep. 2019;9:6371. doi:10.1038/s41598-019-42870-y

[13] Cantor B. Multicomponent and High Entropy Alloys. Entropy. 2014;16 (9):4749–4768. doi:10.3390/e16094749

[14] Hou JX, Liu SF, Cao BX, et al. Designing nanoparticles-strengthened high-entropy alloys with simultaneously enhanced strength-ductility synergy at both room and elevated temperatures. Acta Mater. 2022;238:118216. doi:10.1016/j.actamat.2022.118216

[15] Wen YH, Simmons JP, Shen C, et al. Phase-field modeling of bimodal particle size distributions during continuous cooling. Acta Mater. 2003;51 (4):1123–1132. doi:10.1016/S1359-6454(02)00516-5

[16] Vogel F, Wanderka N, Matsumura S, et al. Early stages of decomposition within the γ' phase of a Ni–Al–Ti model alloy. Intermetallics. 2012;22:226–230. doi:10.1016/j.intermet.2011.11.011

[17] Chen YQ, Francis E, Robson J, et al. Compositional variations for small-scale gamma prime (γ') precipitates formed at different cooling rates in an advanced Ni-based superalloy. Acta Mater. 2015;85:199–206. doi:10.1016/j.actamat.2014.11.009

[18] Liu XS, Li R, Lu Y, et al. Spinodal decomposition induced nanoprecipitates strengthened CoCrNi-base medium entropy alloy. Mater Sci Eng, A. 2021;822:141674. doi:10.1016/j.msea.2021.141674

[19] Tsai KY, Tsai MH, Yeh JW. Sluggish diffusion in Co-Cr-Fe-Mn-Ni high-entropy alloys. Acta Mater. 2013;61 (13):4887–4897. doi:10.1016/j.actamat.2013.04.058

[20] Wang ZG, Zhou W, Fu LM, et al. Effect of coherent $L1_2$ nanoprecipitates on the tensile behavior of a fcc-based high-entropy alloy. Mater Sci Eng, A. 2017;696:503–510. doi:10.1016/j.msea.2017.04.111

[21] Nazaretyan K, Aydinyan S, Kirakosyan H, et al. AlCo-rich AlCoNiFe and AlCoNiFeCr high entropy alloys: Synthesis and interaction pathway at high heating rates. J Alloys Compd. 2023;931:167589. doi:10.1016/j.jallcom.2022.167589

[22] Qiu RS, Luan BF, Chai LJ, et al. Effects of heating rates and alloying elements (Sn, Cu and Cr) on the $\alpha \rightarrow \alpha+\beta$ phase transformation of Zr-Sn-Nb-Fe-(Cu, Cr) alloys. J Nucl Mater. 2014;453 (1–3):269–274. doi:10.1016/j.jnucmat.2014.07.017

[23] Barriobero-Vila P, Requena G, Buslaps T, et al. Role of element partitioning on the α-β phase transformation kinetics of a bi-modal Ti-6Al-6V-2Sn alloy during continuous heating. J Alloys Compd. 2015;626:330–339. doi:10.1016/j.jallcom.2014.11.176

[24] Wu ZC, Xu XF, Zhao Y, et al. Investigation of accelerated recrystallization behavior via electropulsing treatment in CoCrFeMnNi high-entropy alloy. Mater Sci Eng, A. 2023;863:144536. doi:10.1016/j.msea.2022.144536

[25] Yan X, Xu X, Zhou Y, et al. Constructing a novel bi-lamellar microstructure in selective laser melted Ti-6Al-4V alloy via electropulsing for improvement of strength and corrosion resistance. J Met Sci Technol. 2024;193:37–50. doi:10.1016/j.jmst.2023.12.060

[26] Wang YF, Xia L, Cao YT, et al. Imposition of electric current to promote the Portevin-Le Chatelier effect of CoCrFeMnNi high-entropy alloy at low temperatures. Mater Sci Eng, A. 2020;793:139893. doi:10.1016/j.msea.2020.139893

[27] Xu XF, Zhao YG, Ma BD, et al. Rapid precipitation of T-phase in the 2024 aluminum alloy via cyclic electropulsing treatment. J Alloys Compd. 2014;610:506–510. doi:10.1016/j.jallcom.2014.05.063

[28] Wang HR, Kou R, Harrington T, et al. Electromigration effect in Fe-Al diffusion couples with field-assisted sintering. Acta Mater. 2020;186:631–643. doi:10.1016/j.actamat.2020.01.008

[29] Zhu YH, To S, Lee WB, et al. Effects of dynamic electropulsing on microstructure and elongation of a Zn-Al alloy. Mater Sci Eng, A. 2009;501 (1-2):125–132. doi:10.1016/j.msea.2008.09.080

[30] Qin SY, Hao JQ, Yan LG, et al. Ultrafast solution treatment to improve the comprehensive mechanical properties of superalloy by pulsed electric current. Scr Mater. 2021;199:113879. doi:10.1016/j.scriptamat.2021.113879

[31] Laplanche G. Growth kinetics of σ-phase precipitates and underlying diffusion processes in CrMnFeCoNi high-entropy alloys. Acta Mater. 2020;199:193–208. doi:10.1016/j.actamat.2020.08.023

[32] Laplanche G, Berglund S, Reinhart C, et al. Phase stability and kinetics of σ-phase precipitation in CrMnFeCoNi high-entropy alloys. Acta Mater. 2018;161:338–351. doi:10.1016/j.actamat.2018.09.040

[33] Jiang YB, Tang GY, Shek C, et al. On the thermodynamics and kinetics of electropulsing induced dissolution of β-$Mg_{17}Al_{12}$ phase in an aged Mg-9Al-1Zn alloy. Acta Mater. 2009;57 (16):4797–4808. doi:10.1016/j.actamat.2009.06.044

[34] Ben DD, Yang HJ, Dong YA, et al. Cryogenic electropulsing induced microstructure optimization of a cold-rolled CoCrFeMnNi high-entropy alloy. Mater Charact. 2023;195:112557. doi:10.1016/j.matchar.2022.112557

[35] Yang ZQ, Bao JX, Ding CG, et al. Electroplasticity in the $Al_{0.6}$CoCrFeNiMn high entropy alloy subjected to electrically-assisted uniaxial tension. J Met Sci Technol. 2023;148:209–221. doi:10.1016/j.jmst.2022.11.031

[36] Zhao YC, Wan M, Meng B, et al. Pulsed current assisted forming of ultrathin superalloy sheet: Experimentation and modelling. Mater Sci Eng, A. 2019;767:138412. doi:10.1016/j.msea.2019.138412

[37] Zhang X, Li HW, Zhan M. Mechanism for the macro and micro behaviors of the Ni-based superalloy during electrically-assisted tension: Local Joule heating effect. J Alloys Compd. 2018;742:480–489. doi:10.1016/j.jallcom.2018.01.325

[38] Liu YZ, Wan M, Meng B. Multiscale modeling of coupling mechanisms in electrically assisted deformation of ultrathin sheets: An example on a nickel-based superalloy. Int J Mach Tools Manuf. 2021;162:103689. doi:10.1016/j.ijmachtools.2021.103689

[39] Shibkov AA, Denisov AA, Zheltov MA, et al. The electric current-induced suppression of the Portevin - Le Chatelier effect in Al-Mg alloys. Mater Sci Eng, A. 2014;610:338–343. doi:10.1016/j.msea.2014.05.050

[40] Mishin Y. Calculation of the γ/γ' interface free energy in the Ni-Al system by the capillary fluctuation method. Modell Simul Mater Sci Eng. 2014;22 (4):045001. doi:10.1088/0965-0393/22/4/045001

[41] Ardell AJ. Interfacial free energies and solute diffusivities from data on Ostwald ripening. Interface Sci. 1995;3 (2):119–125. doi:10.1007/BF00207013

[42] Tóth GI, Morris JR, Gránásy L. Ginzburg-Landau-Type multiphase field model for competing fcc and bcc Nucleation. Phys Rev Lett. 2011;106 (4):045701. doi:10.1103/PhysRevLett.106.045701

[43] Malik A, Odqvist J, Höglund L, et al. Phase-field modeling of sigma-phase precipitation in 25Cr7Ni4Mo duplex stainless steel. Metall Mater Trans A. 2017;48 (10):4914–4928. doi:10.1007/s11661-017-4214-7

[44] Liao YF, Baker I. On the room-temperature deformation mechanisms of lamellar-structured $Fe_{30}Ni_{20}Mn_{35}Al_{15}$. Mater Sci Eng, A. 2011;528 (12):3998–4008. doi:10.1016/j.msea.2011.01.089

[45] Lu YP, Gao XZ, Jiang L, et al. Directly cast bulk eutectic and near-eutectic high entropy alloys with balanced strength and ductility in a wide temperature range. Acta Mater. 2017;124:143–150. doi:10.1016/j.actamat.2016.11.016

[46] Liu WH, Lu ZP, He JY, et al. Ductile CoCrFeNiMox high entropy alloys strengthened by hard intermetallic phases. Acta Mater. 2016;116:332–342. doi:10.1016/j.actamat.2016.06.063

[47] Xie SY, Zhang JX, Li RD, et al. Accelerated precipitation of the B_2 particles and its effect on $Al_{0.3}$CoCrFeNi high-entropy 1. Abhandlung: Übersättigung und Überkaltung-Modelling and Simulation in Materials Science and Engineeringalloy by electric current assisted annealing. Mater Charact. 2021;181:111434. doi:10.1016/j.matchar.2021.111434

[48] Fan L, Yang T, Zhao Y, et al. Ultrahigh strength and ductility in newly developed materials with coherent nanolamellar architectures. Nat Commun. 2020;11 (1):6240. doi:10.1038/s41467-020-20109-z